Large-eddy simulation of thin film evaporation and condensation from a hot plate in enclosure: Second order statistics

Carlo Cintolesi, Andrea Petronio, Vincenzo Armenio

Large-eddy simulation of thin film evaporation and condensation from a hot plate in enclosure: Second order statistics

Carlo Cintolesi[a,*], Andrea Petronio[b], Vincenzo Armenio[a]

[a] *University of Trieste, Dipartimento di Ingegneria e Architettura, via Alfonso Valerio 10, I-34127 Trieste, Italy*
[b] *IEFLUIDS S.r.l., Piazzale Europa 1, I-34127 Trieste, Italy*

Abstract

The archetypal case of a hot and wet plate surrounded by a cold and wet square enclosure is studied. Turbulent natural convection, the water evaporation/condensation, the heat exchange between the air and the enclosing solid bodies are simulated. The large-eddy simulation methodology is adopted in conjunction with a dynamic Lagrangian model for subgrid scale viscosity and thermal-vapour diffusivities. Two statistical steady state simulations (maximum $Ra = 5 \times 10^8$) and three transitory drying-process simulations are carried out by deactivating and activating the air-solid heat transfer, respectively. The present work extends the companion study of Cintolesi *et al.* [8], where first order statistics of the above mentioned cases were presented. Here, second order statistics are shown: first, the turbulent structures of the thermally uncoupled cases are analysed, along with the velocity root-mean square, the turbulent scalar fluxes and the turbulent kinetic energy budget. A few zones of negative production of turbulent kinetic energy are identified and discussed. The presence of splat and anti-splat events on the enclosure surface is detected and discussed. Subsequently, the evolution of the drying-process simulations is reported: the physical properties of the plate materials lead to different decays of the surface thermal fluctuations.

Keywords: Large-eddy simulations; natural convection; conjugate heat transfer; evaporation and condensation; negative TKE production.

NOTE: this is the final version of the manuscript accepted for publication. Reference to the published article:

Carlo Cintolesi, Andrea Petronio, Vincenzo Armenio. *Large-eddy simulation of thin film evaporation and condensation from a hot plate in enclosure: Second order statistics.* Int. Journal of Heat and Mass Transfer 115 (2017) 410-423. doi: dx.doi.org/10.1016/j.ijheatmasstransfer.2017.08.043.

1. Introduction

The present work extends the analysis reported in the companion paper Cintolesi *et al.* [8] (henceforth CPA16). There a Large-Eddy Simulation (LES) methodology is used to study numerically the archetypal case of a hot and wet vertical plate placed in a cold and wet, square enclosure. In this context, it is worthwhile to mention that the use of LES allows exploiting flow features and high order statistics, not obtainable using standard methods relying on Reynolds-average simulations. The turbulent natural convection arising within the enclosure is reproduced, along with the evaporation from the water film onto the plate, the condensation on the enclosure surfaces and the conjugate heat transfer (CHT) between the air and the solid bodies. Different simulations are carried out. Initially, the CHT is switched off and two thermally uncoupled cases are investigated: the humid air case, where the evaporation-condensation process is allowed and the water film does not change its thickness; the dry air case, where air and solid surfaces are dry (hence evaporation and condensation do not occur). These cases are run until a statistical steady state configurations are reached. Subsequently, the final configuration for the humid air case is used to initialise three transient simulations, in which the CHT is switched on and the film thickness is allowed to vary in time. Such simulations are carried out changing the plate material: steel, PVC and porcelain are used for the plate, while the enclosure is always set of mild steel. The CHT reproduces the cooling of the plate and, consequently, the reduction of fluid motion and water evapora-

*Corresponding author.
Email addresses: carlo.cintolesi@gmail.com (Carlo Cintolesi), a.petronio@iefluids.com (Andrea Petronio), armenio@dica.units.it (Vincenzo Armenio)

tion. The thermal-physical properties of the plate materials strongly influence the cooling process and the overall evolution of the system.

Similar phenomena have been studied in literature, using different simulation techniques. Russo *et al.* [25] used Direct Numerical Simulations (DNS) to study a turbulent droplets-laden channel flows at low Reynolds, where the droplet distribution was simulated using a Lagrangian approach. Bukhvostova *et al.* [4] use the same Lagrangian approach, compering the performance of the incompressible and compressible solver. The discrepancies between the two were minimal for the fluid quantities, but relevant for the thermodynamic quantities. Overall, the compressible solver was more accurate. Laaroussi and Lauriat [18] investigated the thermosolutal convection and condensation of humid air in two-dimensional square cavity case, with thermal coupling between fluid and solid boundaries. A compressible low-Mach approach was adopted and compared with the incompressible Boussinesq assumption: it resulted that both methods gave similar results when the initial temperature was uniform and equal to the average between the hot and cold isothermal walls. Iskra and Simonson [16] performed experiments on the three-dimensional rectangular ducts, both in turbulent and laminar regimes, while Raimundo *et al.* [24] analysed water evaporation and condensation across water free surface (simulations and experiments were performed). The problems related to conjugate heat transfer have been also studied: a review on this subject can be found in Dorfman and Renner [9]; a description of the main numerical coupling strategies is reported by Duchaine *et al.* [11],[12]; while the technique herein used are described and validated by Sosnowski *et al.* [27].

In CPA16 the authors presented the first order statistics and the description of the gross motion for the aforementioned simulations. For the cases named *preliminary cases* in CPA16 and hereafter referred as *thermally uncoupled cases*, the mean flow was described along with the effects of the thermal-vapour stratification. The buoyancy force generated near the hot plate and near the vertical cold enclosure walls drives the flow. Three regions of high-speed motion were identified: (i) the ascending region, just above the plate where the hot air rises from the hot plate; (ii) the horizontal-flow region, near the enclosure horizontal wall (ceiling) where air flows towards the vertical walls of the enclosure; (iii) the descending region, near the upper part of the vertical walls of the enclosure where the buoyancy force pushes air downward. An additional region of low-speed flow, named the diagonal-flow region, appears when air is driven from the descending to the ascending regions across the cavity. A strong stable thermal-vapour stratification sharply splits the cavity into a hot-humid upper part and a cold-dry bottom part. Stratification inhibits air recirculation over the entire cavity height, thus the motions remain confined in the top-half of the cavity. Flow velocity and the stable stratification are more energetic for the humid case than for the dry one. Also, the heat transfer at the solid surfaces were studied, showing that evaporation and condensation rule the fluid-solid heat exchange. For the drying-process cases, the time evolution of active scalars (*i.e.* average temperature and vapour concentration) were reported, together with a description of the main flow characteristics all over the domain and along selected lines. The cooling process has been simulated for $60\,s$ of physical time; this initial interval is crucial to investigate the different evolution of the systems associated to the variation of the plate materials. It was found that the thermal inertia ρC_p of the solid media controls the cooling process: when the average plate temperature is plotted in time, the steel plate (high ρC_p) exhibits a linear and moderate reduction of temperature, while the porcelain plate (low ρC_p) shows a higher cooling, with an initial strong and subsequent moderate decrease of temperature. PVC plate (moderate ρC_p) displays an intermediate behaviour. The evaporation of the water film on the plate and its condensation over the enclosure were also analysed: the water film thickness varies according with the temperature evolution. An estimation of the dew-point temperature showed that re-condensation onto the plate is not allowed, for the materials considered in the study.

In the present study, the development of the turbulent field within the enclosure in the same conditions as in CPA16 is investigated through the analysis of the second order statistics. The knowledge of turbulence is important for understanding the mixing of temperature and water vapour within the cavity, and hence the heat transfer mechanism between the air and the surrounding medium. In the following sections, for sake of completeness, the governing equations and the simulation settings are summarised, and some additional details on the turbulent model not already presented in CPA16. Subsequently, the turbulent structures, the spatial distribution of the turbulent shear stresses, the turbulent scalar fluxes and the thermal fluctuations on solid surfaces are presented. The turbulent kinetic energy budget is also calculated for the thermally uncoupled humid case: three zones of negative production are detected and described.

The paper is organised as follow: section 2 reports the mathematical model, the simulation technique employed and some details on the numerical methods adopted; section 3 illustrates the physical problem that is reproduced, the settings of the cases and the non-dimensional parameters; section 4 shows the second order statistics and the turbulent kinetic energy budget for the thermally uncoupled cases; section 5 reports the instantaneous Reynolds and Rayleigh numbers and the surface thermal fluctuations for the drying-process simulations; in section 6 some final remarks are given.

2. Simulation technique

All the quantities are expressed in the international system of units (SI).

Nomenclature

Latin symbols

ν molecular kinematic viscosity
α molecular thermal diffusivity
ω water vapour concentration
ρ space-time variable density
ρ^* sum of air and vapour density
C_p specific heat coefficient at constant pressure
k thermal conductivity
g gravity acceleration
β expansion coefficient
L_h latent heat of vaporisation
T temperature
H water film thickness
p dynamic pressure
t time
Γ solid-fluid interface
η second invariant of the normalised anisotropy tensor
S_{ij} strain rate tensor
s_{ij} fluctuation strain rate tensor
$S_{s/a}$ heat source/sink due to water change of phase
τ_{ij} stress tensor
c_s^2 Smagorinsky constant for turbulent viscosity
c_t^2 Smagorinsky constant for turbulent diffusivity
k_e turbulent kinetic energy (TKE)
P_K TKE production
B_K TKE buoyancy flux
ϵ_K TKE dissipation
ϵ_{SGS} SGS contribution to TKE
$\mathcal{T}_j$ TKE transport term

Non-dimensional numbers

Pr Prandtl number
Ra Rayleigh number
Re Reynolds number
L characteristic length
U_0 characteristic velocity
t_0 characteristic time
ω_{asy} average vapour concentration in uncoupled case

Subscripts and superscripts

ψ generic variable
ψ' variation from mean value
$\overline{\psi}$ grid space filter
$\widehat{\psi}$ test space filter
ψ_a air related quantity
ψ_s solid related quantity
ψ_v vapour related quantity
ψ_w water related quantity
ψ_p quantity evaluated on the plate
ψ_e quantity evaluated on the enclosure
ψ_T temperature related quantity
ψ_ω vapour concentration related quantity
ψ_0 reference or characteristic value
ψ_{ij} i,j-component, where $i,j = x,y,z$
ψ_{SGS} sub-grid scale quantity
$[\psi]_{\text{RMS}}$ root-main square

Vectors

$\mathbf{g}$ gravity acceleration
$\mathbf{u}$ air velocity
$\mathbf{U}_\omega$ evaporation/condensation velocity
$\mathbf{x}$ position vector

2.1. Governing equations

Air medium is considered incompressible and the Boussinesq approximation is adopted. The buoyancy force is generated by thermal and vapour gradients. The governing equations read:

$$\frac{\partial u_i}{\partial x_i} = 0, \tag{1}$$

$$\frac{\partial u_i}{\partial t} + u_j \frac{\partial u_i}{\partial x_j} = -\frac{1}{\rho_0}\frac{\partial p}{\partial x_i} + \nu \frac{\partial^2 u_i}{\partial x_j \partial x_j} - \frac{\rho}{\rho_0} g \delta_{iy}, \tag{2}$$

$$\frac{\rho}{\rho_0} = 1 - \beta_T (T - T_0) - \beta_\omega (\omega - \omega_0), \tag{3}$$

Vapour concentration is defined as the ratio between vapour mass and the sum of vapour and air masses over a unitary volume, hence $\omega \in [0,1]$. Temperature and vapour concentration are considered active scalars and, in the air medium, they are ruled by the following advection-diffusion equations:

$$\frac{\partial T_a}{\partial t} + u_j \frac{\partial T_a}{\partial x_j} = \alpha_a \frac{\partial^2 T_a}{\partial x_j \partial x_j} + S_a \,, \tag{4}$$

$$\frac{\partial \omega}{\partial t} + u_j \frac{\partial \omega}{\partial x_j} = \alpha_\omega \frac{\partial^2 \omega}{\partial x_j \partial x_j} \,, \tag{5}$$

MATERIAL	air	vapour	pvc	porcelain	steel
C_p	1 005	-	900	750	500
ρ	1.165	-	1 300	260	7 830
k	0.026	-	0.19	2.20	45.30
$\beta \times 10^3$	3.30	630	-	-	-
$\alpha \times 10^5$	2.220	3.29	0.016	1.130	1.160
$\nu \times 10^5$	1.568	-	-	-	-

Table 1: Physical properties of the media. In addition to these: $L_h = 2.26 \times 10^6\ J/kg$, $\rho^* = 1\ kg/m^3$. Data from Ref. [1], except for data of *Poly Vinyl Chloride* (PVC) taken from Ref. [27].

respectively. Temperature in solid media is governed by

$$\frac{\partial T_s}{\partial t} = \alpha_s \frac{\partial^2 T_s}{\partial x_j \partial x_j} + S_s \ . \tag{6}$$

The terms $S_{a/s}$ represent the thermal sink/source due to water evaporation/condensation:

$$S_{a/s} = -\frac{\rho^* L_h}{(\rho\, C_p)_{a/s}} \frac{\partial U_{\omega,i}}{\partial x_i} \,, \tag{7}$$

where $\rho^* = \rho_a + \rho_v$ and the *semi-impermeable* model is adopted to express the evaporation/condensation velocity:

$$\mathbf{U}_\omega = -\frac{\alpha_\omega}{1-\omega_\Gamma} \left(\frac{d\omega}{dn}\Big|_\Gamma \right) \mathbf{n} \,. \tag{8}$$

In order to solve equation (8), the value of ω_Γ has to be provided. It is estimated by a complex empirical formula, that is not here reported for the sake of brevity. We refer to the companion paper CPA16 for a detailed description of the model and an explicit expression of this quantity.

The water phase on the solid surfaces is modelled through the *thin film assumption* (Ref. [21, 30]): the solid walls are covered by a thin water film of thickness H, that increases (decreases) if condensation (evaporation) occurs. The governing equation for H reads:

$$\frac{\partial H}{\partial t} = \frac{\rho_a}{\rho_w} |\mathbf{U}_\omega| \,, \tag{9}$$

The boundary conditions for vapour concentration equation (5) are: constant-value condition if the boundary surface is wet; zero flux condition if the surface is dry. Surfaces are considered dry if H decreases below a threshold value. The boundary condition for temperature performs the CHT between solid and air media: the coupling condition enforces the continuity of temperature and the balance of the heat fluxes at the interface (Ref. Sosnowski *et al.* [27], Cintolesi [5] and Cintolesi *et al.* [6]).

2.2. Dynamic Lagrangian model

The SGS model was not presented in CPA16. The fluid dynamics is solved adopting the LES approach. A general introduction on this subject can be found, for example, in Sagaut [26] and Piomelli [22], while some more details on the formulation here used are reported in Cintolesi *et al.* [5, 7].

The computation grid acts as an implicit spatial filter on the governing equations and generates Sub-Grid Scale (SGS) extra terms. The filter width is equal to the local cell width, computed as $\overline{\Delta} = (\overline{\Delta}_x \overline{\Delta}_y \overline{\Delta}_z)^{1/3}$. The filtering of the equations (1,2,3) leads to SGS stress tensor:

$$\frac{\partial}{\partial x_i} \tau_{ij} = \frac{\partial}{\partial x_i} \left(\overline{u_i u_j} - \overline{u}_i \overline{u}_j \right) , \tag{10}$$

where the overbar denotes filtered quantities. The system is closed using the eddy viscosity assumption and the Smagorinsky model to determine the SGS viscosity:

$$\tau_{ij} - \frac{\delta_{ij}}{3} \tau_{kk} = -2\nu_{\text{SGS}} \overline{S_{ij}} \quad \text{and} \quad \nu_{\text{SGS}} = c_s^2 \overline{\Delta}^2 |\overline{S_{ij}}|, \tag{11}$$

where $\overline{S_{ij}} = (1/2)[(\partial \overline{u}_i/\partial x_j) + (\partial \overline{u}_j/\partial x_i)]$ is the resolved strain rate tensor. The dynamic Lagrangian model for SGS contribution developed by Meneveau *et al.* [20] is adopted in order to compute the Smagorinsky constant. It has been shown in Cintolesi *et al.* [7] that the dynamic approach is suitable for an accurate reproduction of convective flows, characterised by anisotropic and localised turbulence.

In such model, the SGS viscosity is estimated extracting information from bigger scale of motion, using an additional filtering operation of width $\widehat{\Delta} = 2\overline{\Delta}$ on the resolved velocity field. In order to make the computation more stable, an average over a fluid particle trajectory is performed. Since no direction of homogeneity is required, this method allows to tackle problems with arbitrary geometry. The constant is computed through the formula:

$$c_s^2 = \frac{\mathcal{I}_{LM}(\mathbf{x}, t)}{\mathcal{I}_{MM}(\mathbf{x}, t)}. \tag{12}$$

The numerator and the denominator are solution of the following equations:

$$\frac{\partial \mathcal{I}_{LM}}{\partial t} + \overline{u}_k \frac{\partial \mathcal{I}_{LM}}{\partial x_k} = \frac{1}{\text{T}} \left(L_{ij} M_{ij} - \mathcal{I}_{LM} \right) , \tag{13}$$

$$\frac{\partial \mathcal{I}_{MM}}{\partial t} + \overline{u}_k \frac{\partial \mathcal{I}_{MM}}{\partial x_k} = \frac{1}{\text{T}} \left(M_{ij} M_{ij} - \mathcal{I}_{MM} \right) , \tag{14}$$

where $\text{T} = 1.5\overline{\Delta}(\mathcal{I}_{LM}\mathcal{I}_{MM})^{-1/8}$ is the relaxation timescale, while

$$L_{ij} = \widehat{\overline{u}_i \overline{u}_j} - \widehat{\overline{u}}_i \widehat{\overline{u}}_j, \tag{15}$$

$$M_{ij} = 2\overline{\Delta}^2 \left(\widehat{|\overline{S}|\overline{S}_{ij}} - 4|\widehat{\overline{S}}|\widehat{\overline{S}}_{ij} \right) . \tag{16}$$

The angular hat denotes the additional filter operation. Since the constant c_s^2 is assumed to be always positive, a numerical clipping is performed on factors $\mathcal{I}_{LM}$ and $\mathcal{I}_{MM}$ in order to avoid negative values.

This procedure can be extended to the dynamic computation of active scalars SGS contribution, as shown by

Armenio and Sarkar [2]. When implicit filter is applied also to temperature equation (4) and to vapour concentration equation (5), the SGS heat and vapour fluxes appears. They read

$$\frac{\partial}{\partial x_i} h_i = \frac{\partial}{\partial x_i} \left(\overline{T_a u_i} - \overline{T}_a \overline{u}_i \right), \tag{17}$$

$$\frac{\partial}{\partial x_i} \lambda_i = \frac{\partial}{\partial x_i} \left(\overline{\omega u_i} - \overline{\omega}\, \overline{u}_i \right), \tag{18}$$

respectively. Assuming the gradient diffusion hypothesis (Ref. Pope [23]) and the analogy with Smagorisky model for SGS stress tensor, heat fluxes can be expressed by:

$$h_i = -\alpha_{a,\mathrm{SGS}} \frac{\partial \overline{T_a}}{\partial x_i} \quad \text{and} \quad \alpha_{a,\mathrm{SGS}} = c_t^2 \overline{\Delta}^2 |\overline{S_{ij}}|, \tag{19}$$

where $\alpha_{a,\mathrm{SGS}}$ is the SGS thermal diffusivity and c_t^2 is the Smagorinsky constant related to the SGS thermal flux. Such constant is determined by the equation

$$c_t^2 = 2 \frac{\mathcal{J}_{EQ}(\mathbf{x}, t)}{\mathcal{J}_{QQ}(\mathbf{x}, t)}, \tag{20}$$

where the two quantities $\mathcal{J}_{EQ}$ and $\mathcal{J}_{QQ}$ are solution of

$$\frac{\partial \mathcal{J}_{EQ}}{\partial t} + \overline{u}_k \frac{\partial \mathcal{J}_{EQ}}{\partial x_k} = \frac{1}{\mathrm{T}} \left(E_j Q_j - \mathcal{J}_{EQ} \right), \tag{21}$$

$$\frac{\partial \mathcal{J}_{QQ}}{\partial t} + \overline{u}_k \frac{\partial \mathcal{J}_{QQ}}{\partial x_k} = \frac{1}{\mathrm{T}} \left(Q_j Q_j - \mathcal{J}_{QQ} \right), \tag{22}$$

and

$$E_j = \widehat{\overline{u}_j \overline{T}} - \widehat{\overline{u}}_j \widehat{\overline{T}}, \tag{23}$$

$$Q_j = 2\overline{\Delta}^2 \left(\widehat{|\overline{S}| \frac{\partial \overline{T}}{\partial x_j}} - 4 |\widehat{\overline{S}}| \frac{\partial \widehat{\overline{T}}}{\partial x_j} \right). \tag{24}$$

The SGS model for vapour fluxes uses the same formulae already shown for the heat fluxes, where temperature T is replaced by vapour concentration ω. Hence, the equations for SGS vapour fluxes are not explicitly reported.

3. Problem description

The LES methodology performs three-dimensional and unsteady simulations. Figure 1 depicts the case geometry: a cubic cavity contains a rectangular plate (the plate) and is surrounded by a narrow metallic coat (the enclosure). The internal surfaces of the cavity are wet by a thin water film, the plate is hotter than enclosure and humid air fills the domain. Air is driven by the buoyancy forces generated by the thermal-vapour concentration gradients, in correspondence of the plate and the enclosure walls. The domain is made infinitely long in the z-direction by means of periodic conditions. Hence, the mean fluid flow is two-dimensional and develops over the x, y-plane.

The computational grids for the plate (36 864 points), the enclosure (181 760 points), and the fluid domain

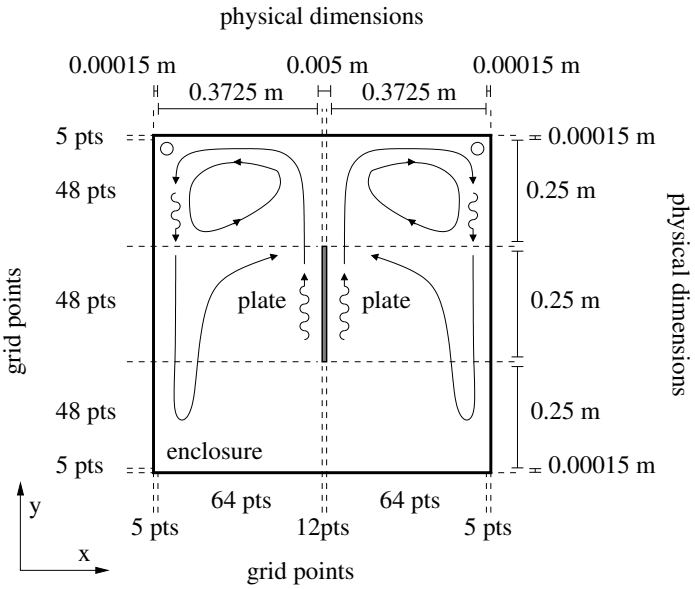

Figure 1: Outline of the case studied and sketch of the main air flow. Bottom-left sides: dimensions of the multi-blocks grids. Top-right sides: geometric dimensions. In z-direction, the cavity is $0.75\,m$ deep and discretised with 64 points.

(1 253 376 points) are obtained with structured, multi-block grids. The structure of the mesh is sketched in Figure 1, along with the physical dimensions of the case. The grid for the fluid domain is stretched near the boundaries in order to directly solve the wall boundary layer. The hyperbolic tangent function proposed by Vinokur [29] is used for the grid stretching. The meshes for the fluid and solid domains are constructed ensuring the same cell dimensions at the fluid-solid interface. The time advancement of the solution is such to obtain a maximum Courant number of $Co = dt|\overline{\mathbf{u}}|/\delta x \leq 0.5$ at each time step dt ($|\overline{\mathbf{u}}|$ is the velocity magnitude through the cell and δx is the cell size in the velocity direction).

3.1. Settings

Different types of simulations were carried out: two thermally uncoupled simulations that reached a statistical steady state configuration, *i.e.* a regime in which the statistics of all quantities do not vary changing the reference time interval; three drying-process simulations that have a transient configuration. In the thermally uncoupled simulations the CHT and water film variations were switched off. The plate temperature ($T_p = 333.15\,K$) was higher than the enclosure one ($T_e = 283.15\,K$) and both were maintained constant in time. The film thickness was $H_i = 0.0001\,m$ and the initial vapour concentration was $\omega = 0$. The evaporation-condensation model was switched off in the dry air case, while it was activated in the humid air case.

With these settings, some concerns arise regarding the validity of the Boussinesq approximation. To the best of

the authors knowledge, a standard criterion to determine the approximation validity is not currently available. Gray and Giorgini [14] suggest that such approximation can be considered valid up a variations of 10% of the thermophysical properties (with respect to the mean value). The variation of density with respect to the mean value is estimated from equation (3) to be $\rho/\rho_0 \cong 12.5\%$ in the thermally uncoupled humid case. Hence, we are reasonably within the range of validity of the Boussinesq approximation.

The drying-process simulations were initialised with the final configuration of the humid air case. The water film thickness was allowed to vary in time and the CHT was turned on: the temperature inside the solid media could change during the process, whereas adiabatic condition were imposed at the external surfaces of the enclosure. Three cases were studied, with three different plate materials and same enclosure made of mild steel. The three materials used are representative of different thermal classes: mild steel (good thermal conductor), PVC (good thermal insulator), porcelain (intermediate behaviour). The main thermal-physical properties of these materials are summarised in Table 1. A discussion on the thermal categories of different materials is reported in Cintolesi *et al.* [7].

3.2. Scales and non-dimensional parameters

Variables are made non dimensional with: the initial difference of temperature $\Delta T = 50\,K$; the initial difference of vapour concentration $\Delta\omega = 0.1255$; the characteristic length $L = 0.375\,m$; the buoyancy velocity $U_0 = \sqrt{(\beta_T \Delta T + \beta_\omega \Delta\omega) g L} \simeq 1\,m/s$; the characteristic time $t_0 = L/U_0 = 0.375\,s$; the asymptotic vapour concentration $\omega_{asy} = 0.025$, that is the fluid average vapour concentration reached in the steady state configuration of thermally uncoupled humid case.

The key non-dimensional parameter in the thermal-vapour convection is the total Rayleigh number.

$$Ra = \frac{g\beta_T}{\nu\alpha_a}\Delta T L^3 + \frac{g\beta_\omega}{\nu\alpha_\omega}\Delta\omega L^2\,, \tag{25}$$

which is composed by the sum of thermal and vapour contributions to the buoyancy force. It expresses the balance between the destabilising effect of buoyancy forces and the stabilising effect of momentum and thermal-vapour diffusion. For drying-process simulations, it is also interesting to analyse the instantaneous Rayleigh number, defined as:

$$Ra(t) = \frac{g\beta_T}{\nu\alpha_a}\left(T_p - T_e\right) L^3 + \frac{g\beta_\omega}{\nu\alpha_\omega}\left[\omega_\Gamma(T_p) - \omega_\Gamma(T_e)\right] L^2\,, \tag{26}$$

where the characteristic temperature of the plate and the enclosure varies in time.

The Reynolds number is defined as the ratio between the inertial and viscous forces, and it is an indicator of the turbulent regime of the flow:

$$Re = \frac{UL}{\nu}\,, \tag{27}$$

where U is the characteristic velocity of the system. In our case, the characteristic buoyancy velocity is used for computing the Reynolds number: $U = U_0$. The instantaneous Reynolds number can be defined as:

$$Re(t) = \frac{U_0(t)L}{\nu} \tag{28}$$

$$= \sqrt{\frac{gL^3}{\nu}\left(\beta_T\left(T_p - T_e\right) + \beta_\omega\left[\omega_\Gamma(T_p) - \omega_\Gamma(T_e)\right]\right)}\,. \tag{29}$$

In section 5 the instantaneous Rayleigh and Reynolds numbers for the drying-process simulations are discussed.

The Rayleigh and Reynolds numbers for the humid air thermally uncoupled simulation are $Ra \cong 5 \times 10^8$ and $Re \cong 2 \times 10^4$, respectively.

4. Results of the thermally uncoupled cases

The second order statistics for the thermally uncoupled simulations where the solid and the fluid media are thermally uncoupled are now discussed. We can underline that these cases are interesting *per se*, regardless the drying cases presented successively, since they reach a statistical steady-state configuration that allows to compute the first- and second-order statistics. Hence, the turbulence features of the fluid flow can be analysed in detail.

We take advantage of the symmetry of the system, flipping the data along the vertical centre-line $x/2L = 0.5$, in order to double the available samples and to improve the statistics. If ψ is a generic variable, then the following notation is adopted in this section: $\langle\psi\rangle$ is the average in time, in z-direction and in left-right side; $\psi' = \psi - \langle\psi\rangle$ is the variable fluctuation; $[\psi]_{RMS} = \sqrt{\langle\psi'\psi'\rangle}$ is the root-mean square (RMS).

In the following sections the second order statistics from the resolved scale of motion are discussed. In general, also the modelled sub-grid scale of motion gives a contribution to such statistics. In LES with eddy viscosity SGS models (either standard or dynamic Smagorinsky model) the contribution of the sub-grid scale stresses are of the order of some percentage with respect to the resolved ones. For a discussion, among the others, ref. [28]. For the present study, the magnitude of the averaged of the isotropic part of the SGS stress tensor (11) for the thermally uncoupled humid case has been scrutinised: the maximum value is two orders of magnitude smaller than the maximum value of the resolved velocity fluctuations (see Figures 3). Hence, we estimate that the SGS contribution to the second order statistics is very small.

4.1. Turbulence structures

The Q-criterion, proposed by Hunt *et al.* [15], is used to visualise the air flow turbulent structures. The name derives from the second invariant of velocity gradient tensor:

$$Q = \frac{1}{2}\left(\Omega_{ij}\Omega_{ij} - S_{ij}S_{ij}\right), \tag{30}$$

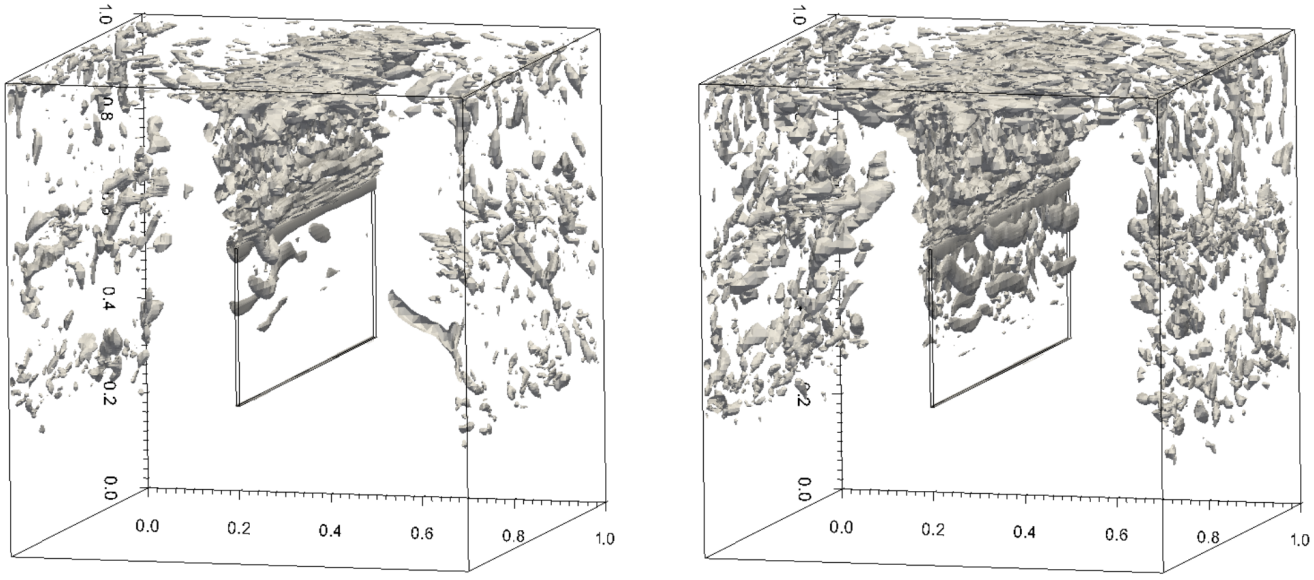

(a) Dry case: isosurfaces $Q = 0.25\,s^{-2}$

(b) Humid case: isosurfaces $Q = 0.25\,s^{-2}$

Figure 2: Coherent vortices for thermally uncoupled cases, visualised with the Q-criterion.

where $\Omega_{ij} = (\partial u_i/\partial x_j - \partial u_j/\partial x_i)/2$. The quantity Q can be interpreted as the balance between rotational rate and strain rate. Thus, the positive isosurfaces of Q are surfaces qualified to delimit vortexes. This method is preferred to others (such as the visualisation of minimum pressure, vorticity or λ_2 isosurfaces) after the analyses of Dubief and Delcayre [10].

Figure 2 presents the isosurface $Q = 0.25\,s^{-2}$ for the humid and dry thermally uncoupled cases. The two cases share the following features:

- Turbulence structures are localised near the boundaries and in the regions of high speed motion: they are more visible in the ascending region above the plate, in the horizontal-flow region near the ceiling, in the descending region near the vertical enclosure walls.
- Near the top part of the vertical plate, vortices appear elongated along the spanwise direction. The coherent structures, in form of rolls, can be detected above the plate and on the plate surface, in the region $0.6 < y/L < 0.8$. Elsewhere, the structures are those typical of convective turbulence.
- In correspondence of the horizontal mid-level ($y/2L = 0.5$) an enhanced turbulence activity is detected near the vertical walls of the enclosure. This is due to the interaction of the main flow with the strong thermal-vapour stratification, that sharply divides the cavity in a top-hot-humid part ($y/2L > 0.5$) and a bottom-cold-dry part ($y/2L < 0.5$).

The main difference between the dry and humid cases is that the former exhibits a sparse population of coherent structures, while the latter has a denser concentration. It can be inferred that the dry case is characterised by a lower level of turbulence with respect to the humid one. This is not surprising after the analysis of the main flow, that is sensibly weaker in absence of vapour concentration gradients.

Fig.	dry air	humid air
3a	$0 < [Ux]_{rms} < 0.086$	$0 < [Ux]_{rms} < 0.128$
3b	$0 < [Uy]_{rms} < 0.084$	$0 < [Uy]_{rms} < 0.105$
3c	$0 < [Uz]_{rms} < 0.109$	$0 < [Uz]_{rms} < 0.140$
5	$0 < [T]_{rms} < 0.144$	$0 < [T]_{rms} < 0.154$
6a	$-0.07 < [UxT]_{rms} < 0.07$	$-0.08 < [UxT]_{rms} < 0.08$
6b	$-0.04 < [UyT]_{rms} < 0.09$	$-0.04 < [UyT]_{rms} < 0.10$

Table 2: Maximum and minimum values of the second order statistics for the dry air and humid air cases. See the relative figures for the notation.

4.2. Space distribution of velocity RMS and turbulent scalar fluxes

The contour-plots of velocity and temperature root-mean square are here discussed, along with the turbulent heat and vapour concentration fluxes. The results for both dry and humid cases are shown. All the statistics are averaged in time and along the spanwise direction, and flipped along the vertical centre-line. The average in time is computed over a period of 5 s of physical time (corresponding to the non-dimensional time $13.33\,t_0$), after that the statistical steady state has been reached. One side of the cavity is reported and commented after the data flipping.

In general, the dry and humid cases exhibit similar features, but the level of fluctuations (quantified by the RMSs of the fluctuating field) is larger in the humid case than in the dry case. As previously mentioned, this is a consequence of the presence of the vapour concentration gradient that enhances convective motion. Table 2 reports the maximum and minimum values of the second order statistics analysed in this section. The velocity RMSs are $20-30\%$ lower in the dry case than in the humid case, the turbulent heat fluxes are 10% lower, while the temperature RMS exhibits a moderate decrease of about 6%. Since the vapour concentration increases the buoyancy force, the velocity RMSs increase much more than the temperature RMSs.

Figure 3 reports the non-dimensional RMSs of the velocity components. They have similar distributions for both dry and humid cases. The horizontal x-component RMS (Figure 3a) reaches the maximum in a thin zone just above the plate, where the plume of hot air starts to enlarge horizontally, and on the ceiling surface above the plate, where the vertical flow impinges on the wall and it is deviated horizontally. The RMS maintains non-zero values in the horizontal-flow region. It becomes sensibly weaker in the descending region and is almost zero elsewhere. A region of very low level of fluctuations is present near the vertical enclosure wall. The RMS of the vertical velocity component (Figure 3b) reaches the climax in the ascending region, above the hot plate, that is the region of most energetic turbulence (see section 4.1). A second zone of relatively high-level turbulence is localised in the lower part of the descending region. The diagonal flow is almost laminar when it merges with the ascending region. Near the ceiling, a narrow boundary layer of low level fluctuations can be detected (see also the discussion of Figure 8b). The RMS of the spanwise velocity component (Figure 3c) exhibits non negligible values in the ascending and descending region. High fluctuations of spanwise velocity can be associated to splat and anti-splat events (ref. Perot and Moin [3]). In order to point out the presence of these events, we look onto the instantaneous velocity field.

Figure 4 displays the instantaneous velocity field, of the last instant simulated of the humid case, onto a horizontal plane near the ceiling ($y/2L = 0.99$). The splat and anti-splat events are clearly visible in the region above the plate (around $x/2L = 0.5$) where the hot air impinges on the ceiling. The vectors of the velocity x, z-components are divergent where splat events occur, while they are convergent where the anti-splat occurs. They are associated to positive and negative values of the vertical velocity, respectively. Also near the vertical enclosure wall, where the flow is deviated downward, the streamlines highlight the presence of vortexes, splat and anti-splat phenomena. High values of spanwise velocity RMS are localised in other two regions within the cavity, near the enclosure vertical wall: at the upper part ($y/2L < 0.9$), they are linked to the presence of the splat and anti-splat events triggered by the horizontal flow that impinges on the enclosure wall; at

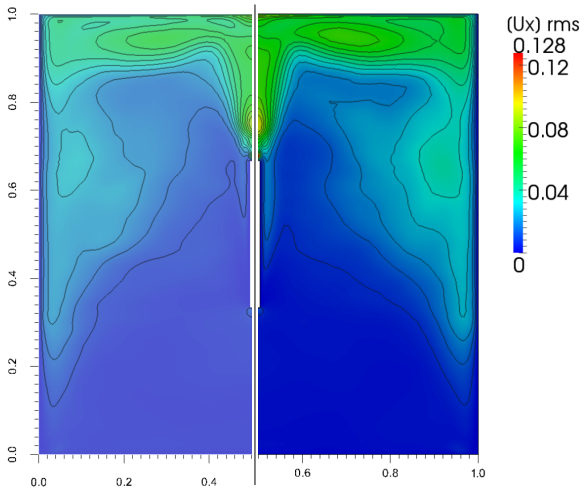

(a) Horizontal velocity RMS, $[U_x]_{rms} = \sqrt{\langle u_x'^2 \rangle}/U_0$.

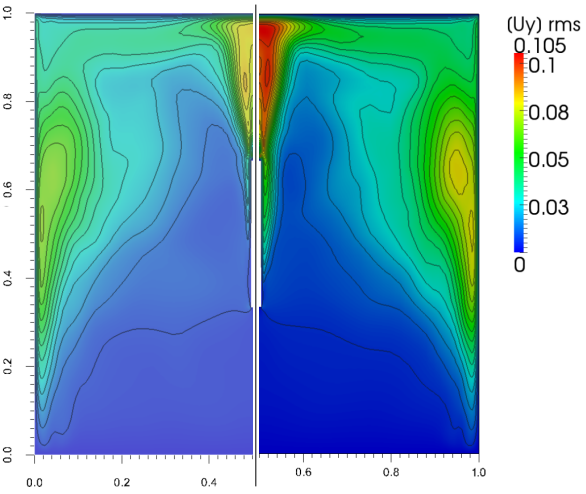

(b) Vertical velocity RMS, $[U_y]_{rms} = \sqrt{\langle u_y'^2 \rangle}/U_0$.

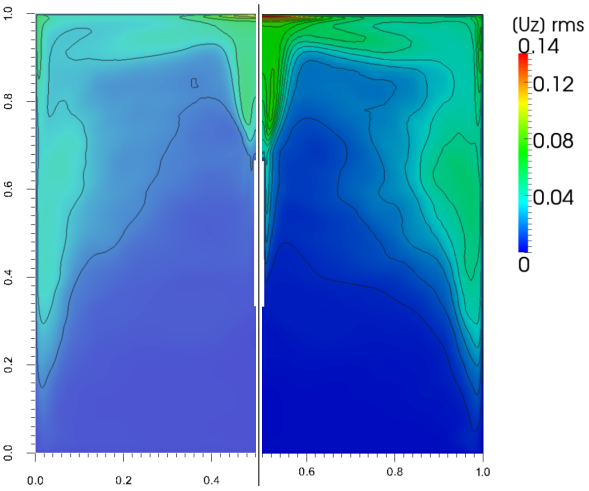

(c) Spanwise velocity RMS, $[U_z]_{rms} = \sqrt{\langle u_z'^2 \rangle}/U_0$.

Figure 3: Contour-plot of velocity components root-mean square of the thermally uncoupled simulations: left, dry case; right, humid case.

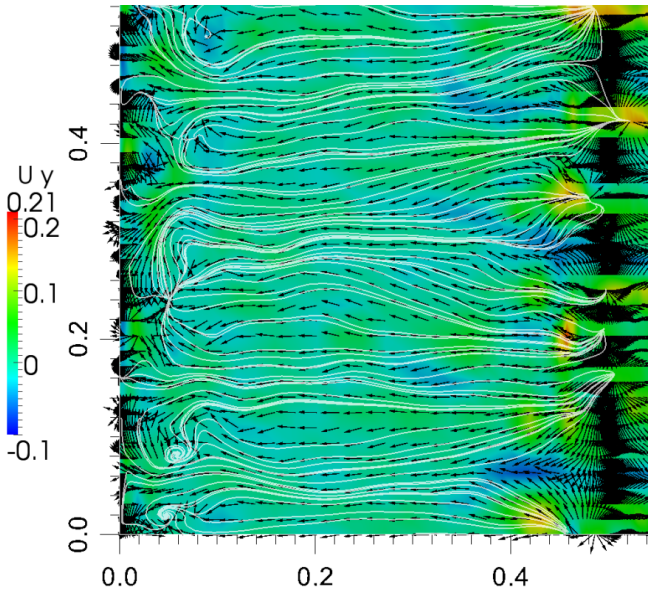

Figure 4: Instantaneous velocity field of humid case, on the x, z-plane at height $y/2L = 0.99$. A square portion $x/2L \times z/2L = 0.52 \times 0.52$ of the plane is shown. The vectors represent the direction of velocity x, z-components on the plane; the magnitude of the velocity y-component is reported as a colour map; the stream-tracers of the velocity field on the plane are also shown.

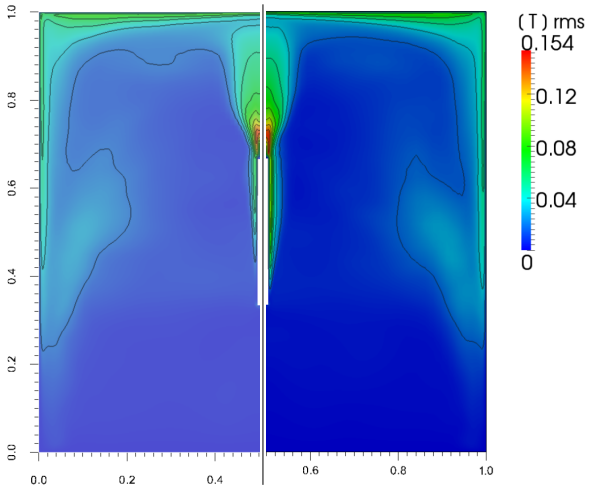

Figure 5: Contour-plot of temperature RMS of the thermally uncoupled simulations, $[T]_{rms} = \sqrt{\langle T'^2 \rangle}/\Delta T$. Left, dry case; Right, humid case.

the mid-height of the cavity, they are given by the upward deflection of the descending flow due to the air stratification.

Figure 5 shows the temperature RMS for dry and humid cases. The temperature RMS in the humid case is slightly higher in magnitude than in the dry case, as a result of the higher level of turbulence in the flow (see Table 2). The two cases exhibit similar features: temperature RMS has its climax above the plate where temperature is transported by the main flow. It is non-zero in a narrow layer near the ceiling and in the upper part of the enclosure vertical walls, where the hot air is cooled down by the enclosure. There is a spot of positive values at the beginning of the diagonal-flow region, where the descending flow from the upper-half of the cavity impinges on the stable thermal (and vapour) stratified fluid at the horizontal mid-line $y/2L = 0.5$. The RMS of vapour concentration for the humid case (here not shown) behaves similarly. This is expected since the vapour and the thermal distribution for thermally uncoupled simulation are ruled by similar equations in absence of CHT (see the discussion in CPA16). However, vapour concentration has substantially higher fluctuations than temperature, essentially because of the high level of water evaporation and condensation.

Figure 6 depicts the turbulent thermal fluxes for the dry and humid cases. Temperature and vapour concentration turbulent fluxes exhibit a similar distribution within the cavity, just temperature fluxes are reported and discussed thus hereafter. The results are interpreted in light of the gradient-diffusion hypothesis (cf. Pope [23]). The horizontal scalar fluxes (Figure 6a) peak in the ascending region. The plume of high/low values is slightly displaced towards the vertical enclosure wall. An additional zone of non-zero fluxes is localised very close to the ceiling surface: the turbulence triggered on the ceiling transports the active scalars in the direction of the horizontal flow. The vertical scalar fluxes (Figures 6b) also are maximum in the ascending region, where the high level of turbulence increases the temperature and vapour transport by turbulent diffusion. They exhibit negative values (weaker in magnitude than the positive ones) in a vertically elongated zone that is approximately coincident with the diagonal-flow region: negative turbulence fluxes are associated with stable thermal-vapour stratification.

4.3. Root-mean square over lines

The non-dimensional RMS of temperature, velocity components and vapour concentration are now reported along a number of selected lines, for both dry and humid cases. The profiles of the dry case are similar to those of the humid case; hence, the common features are discussed and the differences are highlighted wherever present.

In Figure 7 and 8a the RMS of velocity components, temperature and vapour concentration are reported along the three horizontal lines $y/2L = 0.2, 0.5, 0.8$.

Figures 7a and 7b display the velocity RMSs. Close to the enclosure wall and to the plate, they exhibit a rapid growth of the wall-parallel components (u_y and u_z RMS) and a weaker growth of the wall-normal one (u_x RMS). This behaviour indicates the presence of turbulent boundary layer developing because of buoyancy effects near the vertical wall. The vertical velocity RMSs are higher at the mid-level ($y/2L = 0.5$) where the descending flow perturbs the thermal-vapour stratification. In the bottom-level ($y/2L = 0.2$) the RMSs are less intense and the pro-

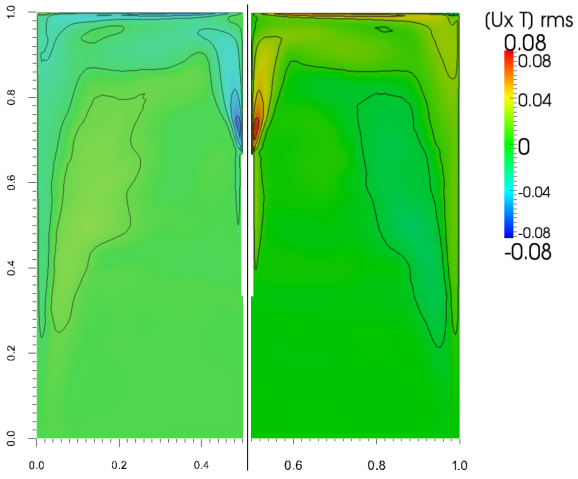

(a) $[UxT]_{rms} = sgn(\langle u'_x T' \rangle)\sqrt{|\langle u'_x T' \rangle|/\Delta T\, U_0}$. Horizontal thermal fluxes: left, dry case; right, humid case.

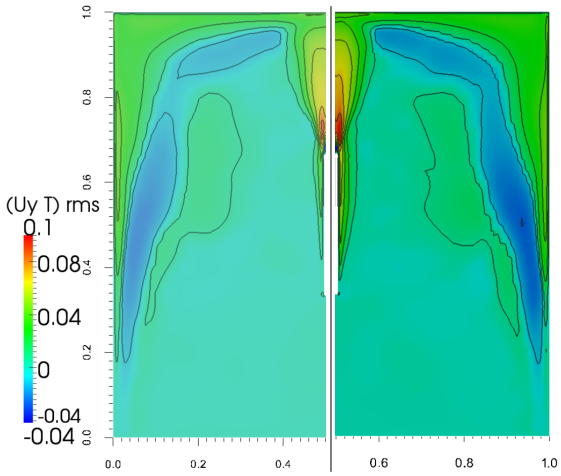

(b) $[UyT]_{rms} = sgn(\langle u'_y T' \rangle)\sqrt{|\langle u'_y T' \rangle|/\Delta T\, U_0}$. Vertical thermal fluxes: left, dry case; right, humid case.

Figure 6: Contour-plot of thermal fluxes of the thermally uncoupled simulations.

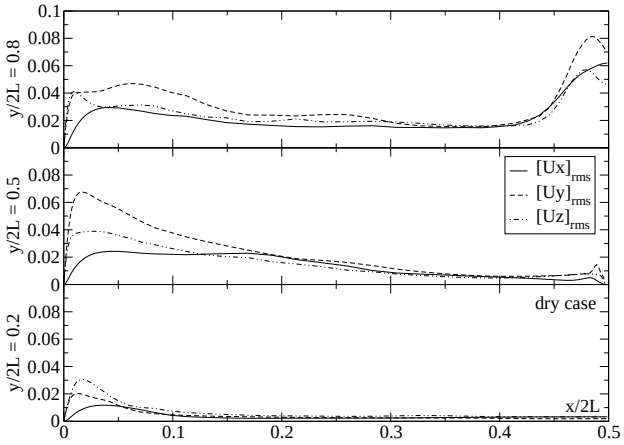

(a) Velocity RMS, dry case.

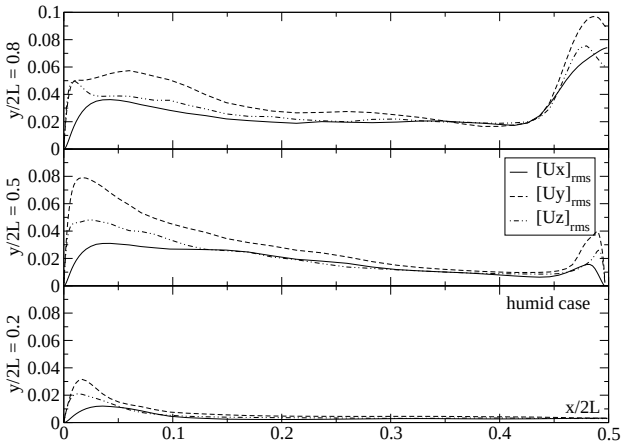

(b) Velocity RMS, humid case.

Figure 7: Non-dimensional RMS of velocity components along selected horizontal lines: $y/2L = 0.2, 0.5, 0.8$. Same notation as in Figure 3 for the variable definitions.

files for the dry case and humid one are almost the same: in the humid case the main stream is stronger than in the dry case, but the same holds for the air stratification; this leads to a similar profile of velocity RMSs in the two cases. Close to the plate, the RMSs of the humid case are sensibly higher than in the dry case, as expected. The RMSs exhibit the near-wall behaviour previously described. Above the plate, along the top-level ($y/2L = 0.8$), the RMSs are slightly higher for the humid case. The RMSs profiles of the velocity components are those typical of a boundary layer, with a monotonic increase near the wall and a smooth decrease beyond a peak value, going far form the wall. The profiles at the top- and mid-level have similar values, because the vertical flow is dominant in the proximity of the wall. The intensity of turbulence decreases going toward the bottom region where the flow is very weak. Here, a residual turbulent boundary layer still exists in proximity of the wall. The intensity of turbulence in the vertical boundary layer is larger in the humid case, due to the already discussed combination of temperature and humidity in the development of buoyancy effects.

Figure 8a reports the temperature and vapour RMS. Humid and dry cases are discussed together, and the vapour RMS profiles are qualitatively similar to those of temperature and are not explicitly discussed. The temperature RMS at the top-level decreases monotonically after the peak near the wall. The presence of the vertical boundary layer is here detectable. At the mid-level, the RMSs start to decrease and then increase again in the range $0.05 < x/2L < 0.2$. This is the zone where the diagonal-flow interacts with the stable stratification. At the bottom-level, the temperature fluctuations are very weak near the wall and decay to zero far from it.

Figure 8b shows the RMSs along a vertical line $x/2L = 0.25$. The velocity RMSs have higher values in the upper part of the cavity ($y/2L > 0.8$) where the energetic convective flow takes place, and they become negligible in the half-bottom part ($y/2L < 0.5$) where the flow is almost at rest. The maximum of the velocity RMSs is reached in the horizontal flow region. The RMS of the wall-parallel components (u_x and u_z RMS) exhibit a local peak very close to the ceiling. However, these peaks are not a consequence of splat and anti-splat events already discussed, since these events are not present in this zone (see Figure 4). Farther from the ceiling, the RMS decreases in correspondence of the diagonal flow ($0.8 \leq y/2L \leq 0.9$), that is nearly laminar. The RMSs are less intense in the dry case and have lower peaks with respect to the humid case in the proximity of the ceiling. Temperature and vapour RMS profiles peak very close to the ceiling (in accordance with Figure 5), where the cooling and condensation effects are higher.

4.4. Turbulence anisotropy

The turbulence anisotropy can be estimated through the normalised anisotropy tensor:

$$b_{ij} = \frac{\langle u_i u_j \rangle}{\langle u_k u_k \rangle} - \frac{1}{3}\delta_{ij}. \qquad (31)$$

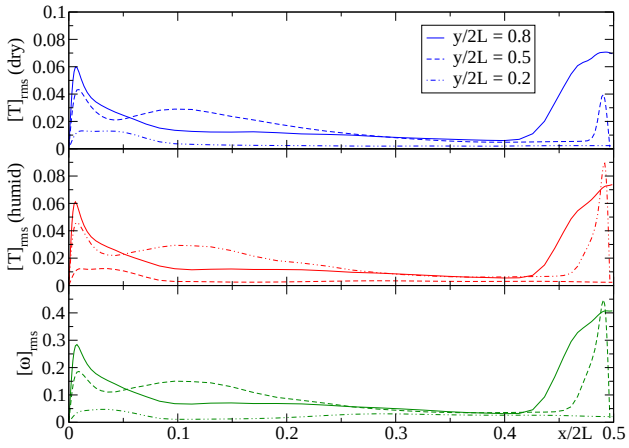

(a) Horizontal lines: $y/2L = 0.2, 0.5, 0.8$.

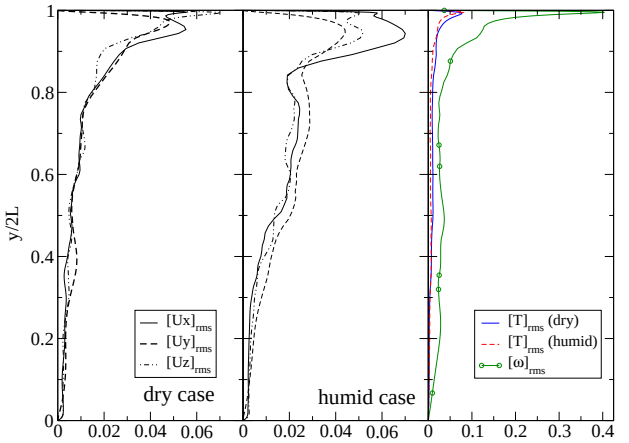

(b) Vertical line $x/2L = 0.25$.

Figure 8: Non-dimensional RMS of temperature, velocity components, and vapour concentration along selected lines. We denote $[\omega]_{rms} = \sqrt{\langle \omega'^2 \rangle}/\omega_{asy}$, see Figure 3 and 5 for the notation of other quantities.

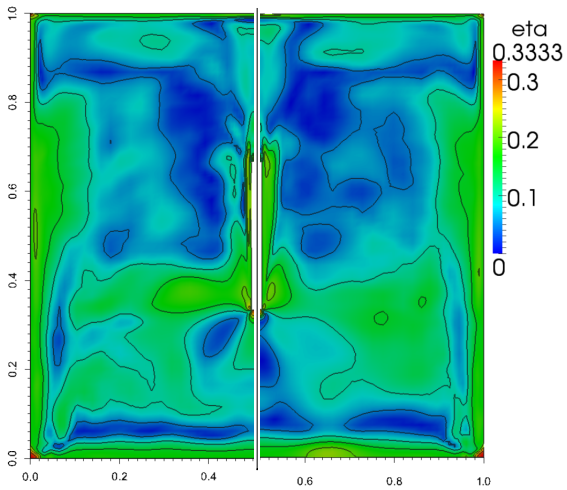

Figure 9: Distribution of the second invariant η of the anisotropy tensor in the cavity. The contour lines are for $\eta = 0, 0.5, 0.1, 0.15, 0.2, 0.25, 0.3$. Left: dry case; right: humid case.

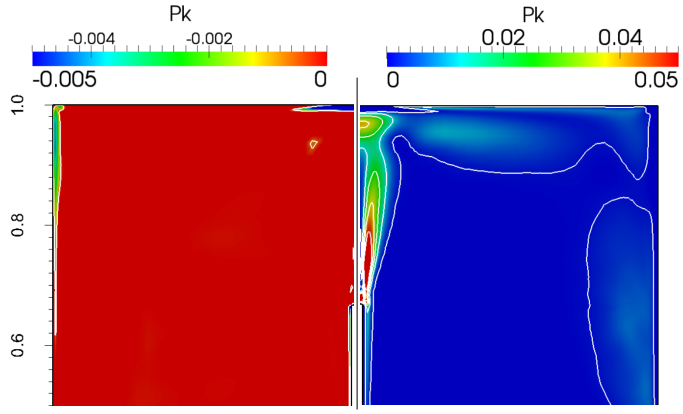

Figure 10: Distribution of negative and positive TKE production in the cavity. The zones highlighted by an appropriate scale. Left: negative production delimited by the contour-plot $P_K = 0$ (white lines). Right: zones of positive production, contour-plot $P_K = 0, 0.01, 0.02, 0.03, 0.05$ (white lines)

The state of anisotropy can be characterised by the second invariant of the tensor, that reads

$$\eta = \sqrt{\frac{1}{6} b_{ii}^2}, \tag{32}$$

following the definition of Pope [23], section 11.3. The variable is limited in the range $\eta \in [0, 1/3]$. where larger values of η denote high anisotropy.

Figure 9 displays the η distribution within the cavity, for dry and humid cases. In both cases the zones of high anisotropy can be localised near the boundaries, as expected. Elsewhere, the two cases exhibit similar features: in the cavity top-half, η is higher in the descending region (where the downward buoyancy force is generated), and it has moderate values in the horizontal flow region. In the cavity bottom-half, the spot of positive values in the cavity centre has to be considered as not relevant, as well as the peak in the corners, since air is almost at rest. The main difference between the two cases is that the humid air shows a wide region of quite high anisotropy near the upper part of the hot plate, while in the dry case this region is reduced to a thin layer close to the plate surface. This is caused by the evaporating water film in the humid case.

4.5. Turbulent kinetic energy

The turbulent kinetic energy (TKE) budget is investigated in this section. The humid thermally uncoupled case is analysed. The energy profiles of the dry case exhibit analogous behaviour with lower values; hence they are not explicitly discussed.

The resolved turbulent kinetic energy $k_e = 1/2\langle u_i' u_i' \rangle$ represents the energy of the resolved fluctuations that can be transported, produced by mean shear, dissipated by viscous effects and produced/destroyed by buoyancy fluxes. It satisfies the following budget

$$\frac{Dk_e}{Dt} = -\frac{d\mathcal{T}_j}{dx_j} + P_K + \epsilon_K + B_K, \tag{33}$$

where $\mathcal{T}_j$ is the transport term (ref. Kundu and Cohen [17] and Pope [23]) and the material derivative is used in the left hand side of the equation. The last three terms are here discussed; they read

$$P_K = -\langle u_i' u_j' \rangle \frac{\partial \langle u_i \rangle}{\partial x_j} \qquad \text{(Production)}, \tag{34}$$

$$B_K = g\langle (\beta_T T' + \beta_\omega \omega')\, u_y \rangle \qquad \text{(Buoyancy flux)}, \tag{35}$$

$$\epsilon_K = -2\nu \langle s_{ij} s_{ij} \rangle - \epsilon_{\text{SGS}} \qquad \text{(Dissipation)}, \tag{36}$$

where $s_{ij} = (1/2)[(\partial u_i'/\partial x_j) + (\partial u_j'/\partial x_i)]$ is the fluctuation strain rate tensor and $\epsilon_{\text{SGS}} = \langle \tau_{ij} \overline{S_{ij}} \rangle + \langle \tau_{ij} \rangle \langle \overline{S_{ij}} \rangle$ is the contribution due to the SGS scales (ref. Armenio and Sarkar [2]).

Figure 10 shows the distribution of the production term P_K within the cavity. Just the top-half cavity is displayed since in the bottom-half of the cavity the level of TKE is substantially negligible. Because of the system symmetry, P_K is equal in the left and right side of the cavity. In order to highlight the zones of negative and positive values, in the left-hand side the negative values are shown, while in the right-hand side just the positive values are displayed. Two zones of high positive production of TKE are localised in correspondence and above of the ascending region. Particularly, in the ascending region the P_K is distributed as two specular plumes, symmetric with respect to the vertical centreline. In between the two plumes, a narrow zone of almost zero production is present. The P_K peaks close to the top horizontal edge of the plate. A few zones of negative production of TKE are also detected. Despite that the production term is usually positive, it is not prevented to assume negative values. In this regards Liberzon *et al.* [19] perform an experimental study of a confined shear flow, in which the negative TKE production is enlightened and discussed considering the presence or the absence of the buoyancy force. Also Gayen and Sarkar [13] studied a stratified oscillating boundary layer on a sloping bottom, pointing out that in this case the reverse stratification can trigger a negative production of TKE.

The three main zones of negative production are:

(a) a horizontally elongated strip close to the ceiling surface, in the range $0.4 < x/2L < 0.6$;

(b) a vertical elongated strip close to the top of the vertical enclosure walls, between $0.861 \lesssim y/2L < 1$;

(c) a narrow boundary layer very close the vertical walls of the plate.

In order to better understand the negative production of TKE, the three terms that compose the P_K are analysed:

$$P_K = -\langle u_x'^2\rangle \frac{\partial\langle u_x\rangle}{\partial x} - \langle u_y'^2\rangle \frac{\partial\langle u_y\rangle}{\partial y} - \langle u_x' u_y'\rangle \left(\frac{\partial\langle u_y\rangle}{\partial x} + \frac{\partial\langle u_x\rangle}{\partial y}\right). \quad (37)$$

The other terms coming form the expansion of equation (34) have almost zero values and do not play a role in the production of TKE, as expected. Moreover, in the three zones under consideration the correlation term decays to zero, $\langle u_x' u_y'\rangle \cong 0$; hence the third term in the above equation is also negligible. In the zone (a), the P_K negative values are due to the horizontal velocity gradient. Indeed, a direct inspection of the terms in equation (37) shows that:

$$P_K\Big|_{zone\ (a)} = -\underbrace{\langle u_x'^2\rangle}_{>0}\underbrace{\partial\langle u_x\rangle/\partial x}_{>0} - \underbrace{\langle u_y'^2\rangle}_{\sim 0}\underbrace{\partial\langle u_y\rangle/\partial y}_{<0}. \quad (38)$$

The averaged spanwise velocity gradient is zero, and the second term becomes negligible since the horizontal velocity fluctuations are almost zero (see also Figure 3a). The sign of the velocity gradient is due to the deflection of the main flow from the vertical to the horizontal direction. At the same distance from the wall and while the left vertical enclosure wall is approached, the production becomes positive since the horizontal velocity decelerates: $\partial\langle u_x\rangle/\partial x < 0$. When the distance from the wall increases, the vertical fluctuations $\langle u_y'^2\rangle$ are not negligible anymore and generate a positive production of TKE. In the zone (b) the negative production comes from the second term of equation (37). Since the main flow is deflected in the vertical direction, we have that

$$P_K\Big|_{zone\ (b)} = -\underbrace{\langle u_x'^2\rangle}_{\sim 0}\underbrace{\partial\langle u_x\rangle/\partial x}_{<0} - \underbrace{\langle u_y'^2\rangle}_{>0}\underbrace{\partial\langle u_y\rangle/\partial y}_{>0}. \quad (39)$$

The horizontal velocity fluctuations are almost zero near the solid surface, hence the first term becomes negligible. The second term is negative since the air decelerates, leading to $\langle u_y\rangle/\partial y > 0$. Downward along the surface, the air is accelerated by the buoyancy generated near the cold wall and the vertical gradient changes sign. In the zone (c) the estimations made in equation (39) are still valid and the negative vertical velocity gradient close to the surface is due to buoyancy force triggered close to the plate surface.

In conclusion, the negative production of TKE localised in zones (a) and (b) is a consequence of the main flow deviation, while in zones (c) it is an effect of the buoyancy force. In all the zones, the negative P_K occurs within a layer close to the solid surfaces, where the velocity fluctuations in the wall-normal direction are almost negligible.

Figure 11a shows the TKE budget along two horizontal lines in the top-half cavity. At the top level ($y/2L = 0.8$) near the enclosure, the production term takes slightly negative values: it corresponds to the zone (b) previously

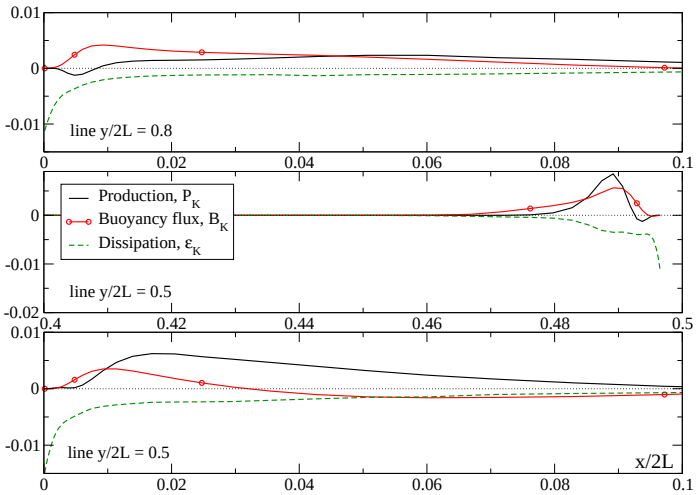

(a) TKE budget along horizontal lines. Top: line $y/2L = 0.8$ near the enclosure; middle: line $y/2L = 0.5$ above the plate; bottom: line $y/2L = 0.5$ near the enclosure.

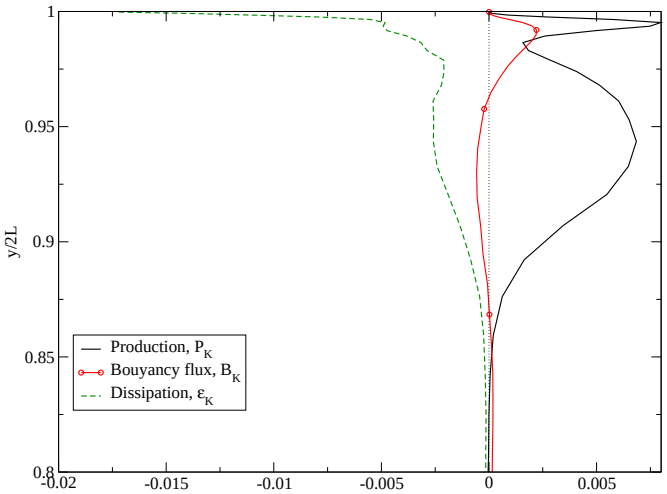

(b) TKE along the line $x/2L = 0.25$, near the ceiling.

Figure 11: TKE budget along selected lines for the humid thermally uncoupled simulation.

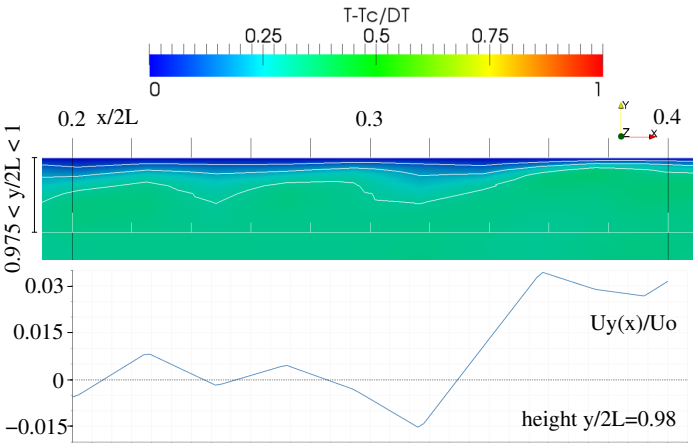

Figure 12: Instantaneous temperature waves close to the ceiling, in the range $0.2 < x/2L < 0.4$. Top: distribution and contour-plot of non-dimensional temperature close to the ceiling ($y/2L > 0.975$). Bottom: non-dimensional vertical velocity profile along the horizontal line $y/2L = 0.98$.

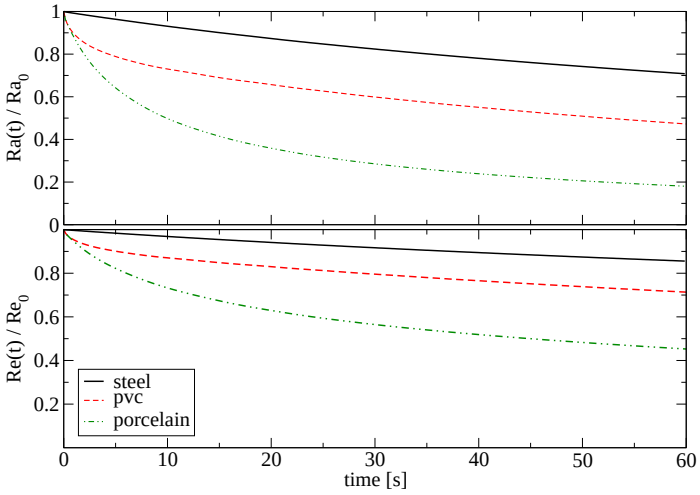

Figure 13: Time evolution of the normalised Rayleigh (top plot) and Reynolds (bottom plot) numbers for the drying-process simulations.

described. The dissipation of the TKE is supported by the buoyancy term. Farther for the wall ($x/2L > 0.01$), the B_K contribution decreases and P_K assumes a positive value. At the mid-high level ($y/2L = 0.5$) near the plate, we can notice the slightly negative production relative to the zone (c). The positive buoyancy flux and production are higher than the viscous dissipation, hence a negative transport of TKE (not reported) occurs. In the mid-high line near the enclosure, the buoyancy production has positive values near the surface and becomes a dissipation term farther from the wall. This can be due to the presence of the diagonal flow that drives air against the stable thermal-vapour stratification.

Figure 11b displays the TKE budgets along a vertical line $x/2L = 0.25$ near the ceiling. The production term in the TKE budget shows a local minimum close to the ceiling, after the peak values ($y/2L \cong 0.98$). Analysing the equation (37), it turns out that the third term of the equation decreases P_K: in correspondence of the minimum, positive values of the fluctuations correlation $\langle u'_x u'_y \rangle > 0$ are associated to high values of strain rate tensor $S_{xy} \gg 0$. Farther from the wall, P_K increases because the S_{xy} decays to zero and the third term becomes negligible.

The minimum point of TKE production, above described, can be caused by the presence of thermal-vapour waves in the region close to the ceiling. Figure 12 displays the instantaneous temperature distribution and the vertical velocity profile in the horizontal flow region, near the ceiling. In this zone, a reverse thermal-vapour stratification occurs since a thin layer of cold and dry air is generated above the hot and humid main flow. The vertical velocity profile shows that the unstable stratification triggers waves of small magnitude (with respect to the main flow). To this concern, Gayen and Sarkar [13] pointed out that the reverse thermal stratification can also cause the negative production of TKE. In their case, the third term in equation (37) is not negligible but it assumes negative values and overcomes the others.

5. Drying-process cases results

This section discusses the turbulent statistics of the three drying-process simulations. From here on, the angular brackets $\langle \psi \rangle$ indicate the average in $z-$direction and time, over an interval $\Delta t = 1\,s$ of physical time (as in CPA16 for the analysis of transient simulations).

5.1. Instantaneous evolution of Rayleigh and Reynolds numbers

The instantaneous Rayleigh (26) and Reynolds (29) numbers are now discussed. The evolution of such non-dimensional numbers is tracked for one minute of physical time (the period simulated for the drying-process cases) corresponding to $160\,t_0$ in non-dimensional time. They are computed using as temperature scale ΔT the difference between the average temperature of the plate T_p, and the average temperature of the vertical walls of the enclosure T_e. They are normalised using the values of Ra and Re of the humid thermally uncoupled simulations, *i.e.*

$$Ra_0 = 4.56 \times 10^8 \quad \text{and} \quad Re_0 = 2.26 \times 10^4, \qquad (40)$$

respectively.

Figure 13 shows the time variation of the above-mentioned normalised non-dimensional numbers. As expected, both decay when the temperature difference decreases and can be interpreted in conjunction with Figure 6 of CPA16, where the time evolution of the average plate temperature is reported. The reduction of the instantaneous Rayleigh number is strongly correlated to the

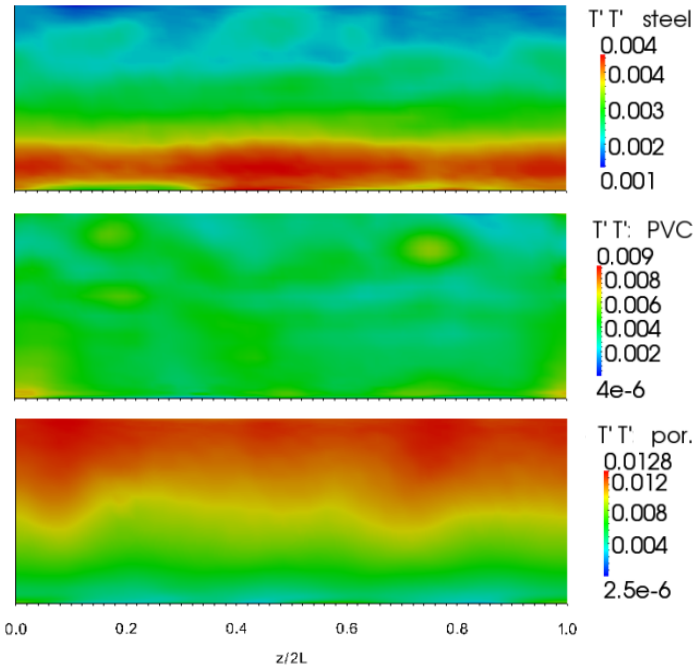

Figure 14: Square of temperature fluctuations onto the vertical plate wall for the three drying-process simulations. The square of the fluctuation is used for a better visualisation.

average plate temperature: the steel case exhibits an almost linear reduction, while the PVC and porcelain cases are characterised by an initial strong decay followed by a quasi-linear decreasing. The instantaneous Reynolds number shows a similar behaviour, with a smoother decrease with respect to $Ra(t)$. In the porcelain case Re drops to about 45% of the initial value, while in the steel and PVC cases it does not go below the 70% of the initial values.

The decay of turbulence (quantified through the time variation of Re and Ra) is strongly connected to the thermal inertia of the hot plate, since it is the main parameter controlling the plate cooling process. However, it depends also on other elements like the solid thermal diffusivity that influences the internal temperature gradient, the intensity of the air flow around the plate that cools down the surface, the thermal conductivities that govern the heat exchange between the air and solid media. Moreover, the complexity and the interconnection of the processes that play a role in the plate cooling, do not allow to find a simple relationship between ρC_p of the plate material and the reduction of turbulence. Qualitatively, large thermal inertia gives low decay of turbulence of the air flow.

5.2. Surface temperature fluctuations

The temperature fluctuations on the plate and the ceiling surfaces, at time $t = 60s$, are discussed in this section. This is the final time for all the drying-process simulations.

Figure 14 shows the fluctuations of T on the vertical plate surface. The three materials exhibit different behaviour, mainly ruled by thermal inertia (see Table 1 for the ρC_p values) and internal temperature distribution (see Figure 10 of CPA16). Steel case maintains a higher internal temperature and the thermal fluctuations are localised in the bottom part of the plate, where the cold and dry air from the bottom-half cavity impinges on the plate. Among the materials studied, steel has the highest ρC_p, hence it is less susceptible to change its temperature and exhibits lower temperature fluctuations. PVC case displays a homogeneous distribution, according to the internal temperature distribution. The fluctuations peak at the bottom corner of the plate. Porcelain case exhibits a behaviour opposite to that of steel case: the plate is cold in the lower part, where the fluctuations are highly reduced. In the upper part, the low specific heat capacity allows for high thermal fluctuations, since the material changes its temperature quickly.

Figure 15 displays the thermal fluctuations onto the ceiling surface. The different behaviour of materials is due to the temperature of the hot plume that rises from the plate. Steel case produces the higher fluctuations, as a result of the high temperature of the air plume. Figure 15a shows a distribution of isolated spots, that are concentrated in the impinging area. PVC case generates an analogous configuration, while porcelain case gives rise to a more homogeneous distribution: a number of small, low intensity, thermal fluctuations are presented all-over the ceiling. This is caused by the low temperature and the weak flow of the air, that does not generate a central zone of high fluctuations.

6. Conclusions

The evaporation and condensation processes from a hot plate in a cold enclosure is investigated using large-eddy simulations. This work is an extension of Cintolesi *et al.* [8] and focuses on the analysis of the second order statistics and turbulent features. The data-set here analysed was generated using LES with the Lagrangian dynamic model to compute the sub-grid scale contributions in the momentum and active scalar equations. The water film onto the surfaces was modelled with the thin film assumption (Petronio [21]). The air-solid heat exchange was computed through a conjugate heat transfer technique and through an explicit source/sink term for water change of phase. The customised numerical solver was developed within OpenFOAM - version 2.1.

First, two statistical steady state thermally uncoupled simulations (with dry and with humid air) setting isothermal walls and a constant water film thickness were performed. Subsequently, they were used to initialised three simulations whit conjugate heat transfer and variable water film thickness. In such cases, the internal plate is made of three materials having different thermo-physical properties: mild steel, PVC and porcelain. The plate drying process was studied in light of the properties of such materials for one minute of physical time ($160\, t_0$).

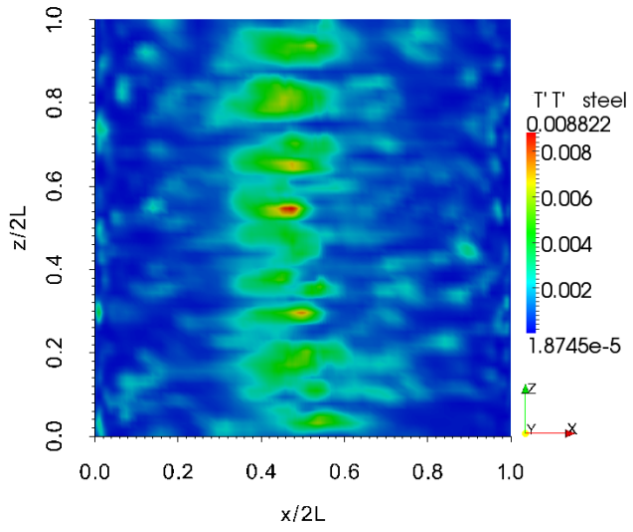

(a) Steel.

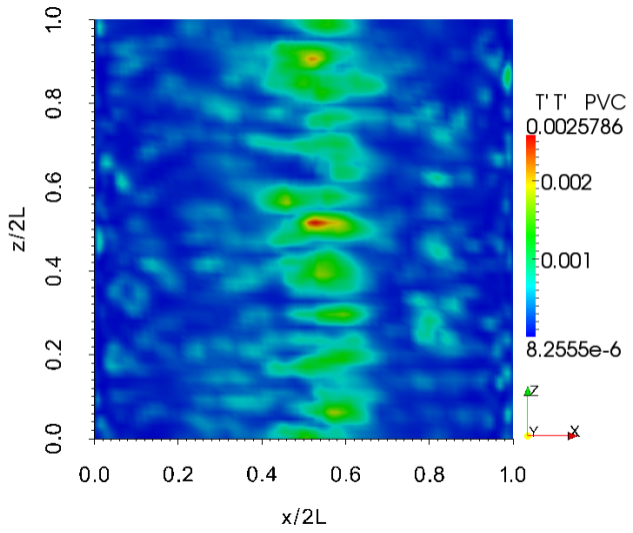

(b) PVC.

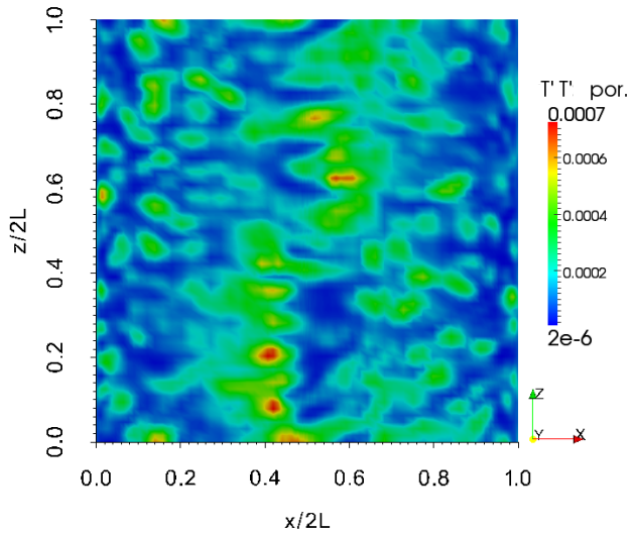

(c) Porcelain.

Figure 15: Square of temperature fluctuations onto the fluid-ceiling interface, for the drying-process simulations. The square of the fluctuation is used for a better visualisation.

Regarding the thermally uncoupled simulations, in the dry case lower level of turbulence is present because of the weaker flow, while in the humid case water vapour increases the buoyancy force and enhances the turbulent convective flow. The Q-criterion was used to visualise the turbulent structures: they are mainly localised in the top-half on the cavity, near the boundaries and in correspondence of the sharp thermal (and vapour) stratification. Just above the hot plate, they have a rolls-like structure elongated in the spanwise direction. The velocity root-mean square shows that the highest level of turbulence is concentrated above the plate and at the cavity mid-height, where the convective flow interacts with the air stratification. Splat and anti-splat events are identified in the top corner region and at the ceiling surface, where a hot air plume impinges on the enclosure. These events give rise to higher values of spanwise velocity root-mean square.

Three regions of negative production of turbulent kinetic energy are identified. A direct inspection of production terms shows that the negative values are due to two phenomena: the deflection of the main flow from vertical to horizontal (and vice versa) direction, and the near-boundary flow acceleration due to the buoyancy force.

Regarding the drying-process cases, materials with higher ρC_p have lower level of temperature fluctuations onto the vertical surface of the plate. In the porcelain case, the bottom half of the plate is almost cold, as fluctuations are mainly localised in the top half. The thermal fluctuations on the enclosure ceiling are associated to the air main flow: a fast and hot air plume leads to high fluctuations localised in the impinging region (steel and PVC cases), while a weak and cold air plume leads to low intensity fluctuations spread across the ceiling surface (porcelain case).

Acknowledgements

This work was supported by Regione Friuli-Venezia Giulia - DITENAVE - Progetto “CFD open source per opera morta - COSMO” n. CUP J94C14000090006.

References

[1] *ASHRAE Handbook Fundamentals - SI edition*, Ed. Ashrae, 2005.

[2] V. Armenio and S. Sarkar, *An investigation of stably stratified turbulent channel flow using large-eddy simulation*, J. Fluid Mechanics, 459 (2002), p. 1.

[3] P. M. Blair Perot, *Shear-free turbulent boundary layers. part 1. physical insights into near-wall turbulence*, Journal of Fluid Mechanics, 295 (1995), p. 199.

[4] A. Bukhvostova, E. Russo, J. Kuertena, and B. Geurts, *Comparison of dns of compressible and incompressible turbulent droplet-laden heated channel flow with phase transition*, Int. J. of Heat and Fluid Flow, 50 (2014), p. 445.

[5] C. Cintolesi, *Large-eddy simulations of conjugate heat transfer with evaporation-condensation and thermal radiation*, Ph.D. thesis, University of Trieste, School of Environmental and Industrial Fluid Mechanics, 29 April 2016. NBN: to be assigned.

[6] C. Cintolesi, H. Nilsson, A. Petronio, and V. Armenio, *Numerical simulation of conjugate heat transfer and surface radiative heat transfer using the p_1 thermal radiation model: parametric study in benchmark cases*, International Journal of Heat and Mass Transfer, 107 (2017), p. 956.

[7] C. Cintolesi, A. Petronio, and V. Armenio, *Large eddy simulation of turbulent buoyant flow in a confined cavity with conjugate heat transfer*, Physics of fluids, 27 (2015).

[8] C. Cintolesi, A. Petronio, and V. Armenio, *Large-eddy simulation of thin film evaporation and condensation from a hot plate in enclosure: First order statistics*, International Journal of Heat and Mass Transfer, 101 (2016), p. 1123.

[9] A. Dorfman and Z. Renner, *Conjugate problems in convective heat transfer: Review*, Mathematical Problems in Engineering, 2009 (2009).

[10] Y. Dubief and F. Delcayre, *On coherent-vortex identification in turbulence*, Journal of Turbulence, 1 (2000), p. 11.

[11] F. Duchaine, A. Corpron, L. Pons, V. Moureau, F. Nicoud, and T. Poinsot, *Development and assessment of a coupled strategy for conjugate heat transfer with large eddy simulation: application to a cooled turbine blade*, Int. J. Heat and Fluid Flow, 30 (2009), p. 1129.

[12] F. Duchaine, S. Mendez, F. Nicoud, A. Corpron, V. Moureau, and T. Poinsot, *Conjugate heat transfer with large eddy simulation for gas turbine components*, Comptes Rendus Mecanique, 337 (2009), p. 550.

[13] B. Gayen and S. Sarkar, *Negative turbulent production during flow reversal in a stratified oscillating boundary layer on a sloping bottom*, Physics of Fluids, 23 (2011).

[14] D. D. Gray and A. Giorgini, *The validity of the boussinesq approximation for liquids and gases*, Int. J. Heat Mass Transfer, 19 (1976), pp. 545–551.

[15] J. C. R. Hunt, A. A. Wray, and P. Moin, *Eddies, stream, and convergence zones in turbulent flows*, Proceedings of the Summer Program - N89-24555. Center For Turbulence Research.

[16] C. Iskra and C. Simonson, *Convective mass transfer coefficient for a hydrodynamically developed airflow in a short rectangular duct*, Int. J. of Heat and Mass Transfer, 50 (2007), p. 2376.

[17] P. Kundu and I. M. Cohen, *Fluid Mechanics*, Elsevier Academic Press, third ed., 2004.

[18] N. Laaroussi and G. Lauriat, *Conjugate thermosolutal convection an condensation of humid air in cavity*, Int. J. Thermal Sciences, 47 (2008), p. 1571.

[19] A. Liberzon, B. Lüthi, M. Guala, W. Kinzelbach, and A. Tsinober, *Experimental study of the structure of flow regions with negative turbulent kinetic energy production in confined three-dimensional shear flows with and without buoyancy*, Physics of Fluids, 17 (2005).

[20] C. Meneveau, T. Lund, and W. Cabot, *A lagrangian dynamic subgrid-scale model of turbulence*, J. Fluid Mechanics, 316 (1996), p. 353.

[21] A. Petronio, *Numerical investigation of condensation and evaporation effects inside a tub*, Ph.D. thesis, School of Environmental and Industrial Fluid Mechanics, University of Trieste, 2010. NBN urn:nbn:it:units-9122.

[22] U. Piomelli, *Large-eddy and direct simulation of turbulent flows*, CFD2001 - 9th Conférence Annuelle de la Société Canadienne de CFD, 2001.

[23] S. Pope, *Turbulent Flows*, Cambridge University Press, 2000.

[24] A. Raimundo, A. Gaspar, A. Virgílio, M. Oliveira, and D. Quintela, *Wind tunnel measurements and numerical simulations of water evaporation in forced convection airflow*, Int. J. of Thermal Sciences, 86 (2014), p. 28.

[25] E. Russo, J. Kuerten, C. van der Geld, and B. Geurts, *Modeling water droplet condensation and evaporation in dns of turbulent channel flow*, J. of Physics Conference Series, 318 (2011).

[26] P. Sagaut, *Large eddy simulation for incompressible flows. An introduction*, Springer, 2000.

[27] P. Sosnowski, A. Petronio, and V. Armenio, *Numerical model for thin liquid film with evaporation and condensation on solid surfaces in a systems with conjugated heat transfer*, Int. J. Heat and Mass Transfer, 66 (2013), p. 382.

[28] V. A. Stefano Salon and A. Crise, *A numerical investigation of the stokes boundary layer in the turbulent regime*, Journal of Fluid Mechanics, 570 (2007), pp. 253–296.

[29] M. Vinokur, *On one-dimensional stretching functions for finite-difference calculations*, Journal of Computational Physics, 50 (1983), p. 215.

[30] J. Welty, C. Wicks, R. Wilson, and G. Rorrer, *Fundamentals of momentum, heat, and mass transfer*, John Wiley and Sons Inc., 5th ed., 2008.